New Degrees of Freedom in Computational Mechanics: Mesh Free Finite Point Method, Rotation Free Shell Triangles and Moving Free Meshes

Eugenio Oñate

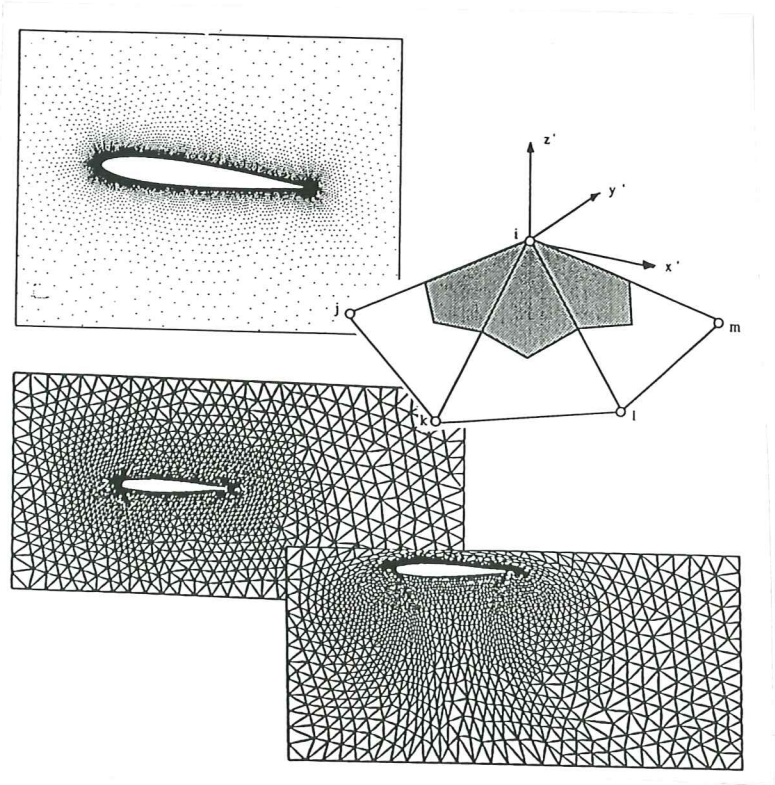

Publication CIMNE Nº 154, January 1999

New Degrees of Freedom in Computational Mechanics: Mesh Free Finite Point Method, Rotation Free Shell Triangles and Moving Free Meshes

Eugenio Oñate

Publication CIMNE Nº 154, January 1999

Plenary lecture at NAFEMS World Congress'99,
Marriot Hotel, Newport, Rhode Island, USA
25-28 April, 1999

International Center for Numerical Methods in Engineering
Gran Capitán s/n, 08034 Barcelona, Spain

NEW DEGREES OF FREEDOM IN COMPUTATIONAL MECHANICS: MESH FREE FINITE POINT METHOD, ROTATION FREE SHELL TRIANGLES AND MOVING FREE MESHES

Eugenio Oñate

SUMMARY

The paper presents an overview of some recent developments in computational mechanics introducing new degrees of "freedom" allowing the solution of more challenging problems. First avances in the finite point method for fully mesh free solution in fluid and solid mechanics are described. Next, new rotation free shell triangles incorporating membrane and bending effects are presented. Finally a simple method allowing free movement of meshes is described. Examples of application of all the "free" methods are given.

1. INTRODUCTION

Considerable effort has been spent in recent years in trying to introduce greater flexibility and simplicity in classical numerical methods, such as the finite element method, for solving a wider range of engineering problems. Some goals aimed by the new procedures are the possibility of elliminating the burden of mesh generation, the use of new simple shell triangles adequate for large scale structural analysis and the efficient update of mesh nodes for problems involving fluid-structure interaction among others.

The paper describes recent advances in the three above mentioned fields. First, progress in the so called finite point method for a fully mesh free solution of problems in fluid and solid mechanics is presented. Next, new rotation free shell triangles adequate for parallel computing of large scale structural problems such as vehicle crash worthiness and sheet metal forming are described. Finally a simple method for free movement of mesh nodes minimizing element distortion is presented. Examples of application of the three "free" techniques are given.

International Centre for Numerical Methods in Engineering,
Universidad Politécnica de Cataluña,
Gran Capitán s/n, 08034 Barcelona, Spain

2. ADVANCES IN THE FINITE POINT METHOD FOR MESH FREE ANALYSIS IN FLUID AND SOLID MECHANICS

Mesh free techniques have become quite popular in computational mechanics. A family of mesh free methods is based on smooth particle hydrodynamic procedures. [1,2]. These techniques, also called free lagrangian methods, are typically used for problems involving large motions of solids and moving free surfaces in fluids. A second class of mesh free methods derive from generalized finite difference (GFD) techniques [3,4]. Here the approximation around each point is typically defined in terms of Taylor series expansions and the discrete equations are found by using point collocation. Among a third class of mesh free techniques we find the so called diffuse element (DE) method [5], the element free Galerking (EFG) method [6,7] and the reproducing kernel particle (RKP) method [8,9]. These three methods use local interpolations for defining the approximate field around a point in terms of values in adjacent points, whereas the discretized system of equations is typically obtained by integrating the Galerkin variational form over a suitable background grid.

The *finite point method* (FPM) proposed in [10–13] is a truly meshless procedure. The approximation around each point is obtained by using standard moving least square techniques similarly as in DE and EFG methods. The discrete system of equations is obtained by sampling the governing differential equations at each point as in GFD methods.

The basis of the success of the FPM for solid and fluid mechanics applications is the *stabilization* of the discrete differential equations. The stable form found by the *finite element calculus* procedure presented in [14–17] corrects the errors introduced by the point collocation procedure, mainly next to the boundary points [13]. In addition, it introduces the necessary stabilization for treating high convection effects and it also allows equal order velocity-pressure interpolations in fluid flow problems. A brief summary of the stabilized FPM is given below.

Interpolation in the FPM

Let Ω_i be the interpolation domain (cloud) of a function $u(x)$ and let s_j with $j = 1, 2, \cdots, n$ be a collection of n points with coordinates

$x_j \in \Omega_i$. The unknown function u may be approximated within Ω_i by

$$u(x) \cong \hat{u}(x) = \sum_{l=1}^{m} p_l(x)\alpha_l = \mathbf{p}(x)^T \boldsymbol{\alpha} \tag{1}$$

where $\boldsymbol{\alpha} = [\alpha_1, \alpha_2, \cdots \alpha_m]^T$ and vector $\mathbf{p}(x)$ contains typically monomials, hereafter termed "base interpolating functions", in the space coordinates ensuring that the basis is complete. For a 2D problem we can specify

$$\mathbf{p} = [1, x, y]^T \quad \text{for} \quad m = 3 \tag{2}$$

and

$$\mathbf{p} = [1, x, y, x^2, xy, y^2]^T \quad \text{for} \quad m = 6 \qquad \text{etc.} \tag{3}$$

Function $u(x)$ can now be sampled at the n points belonging to Ω_i giving

$$\mathbf{u}^h = \begin{Bmatrix} u_1^h \\ u_2^h \\ \vdots \\ u_n^h \end{Bmatrix} \cong \begin{Bmatrix} \hat{u}_1 \\ \hat{u}_2 \\ \vdots \\ \hat{u}_n \end{Bmatrix} = \begin{Bmatrix} \mathbf{p}_1^T \\ \mathbf{p}_2^T \\ \vdots \\ \mathbf{p}_n^T \end{Bmatrix} \boldsymbol{\alpha} = \mathbf{C}\boldsymbol{\alpha} \tag{4}$$

where $u_j^h = u(x_j)$ are the unknown but sought for values of function u at point j, $\hat{u}_j = \hat{u}(x_j)$ are the approximate values, and $\mathbf{p}_j = \mathbf{p}(x_j)$.

In the FE approximation the number of points is chosen so that $m = n$. In this case $\mathbf{C}$ is a square matrix. The procedure leads to the standard shape functions in the FEM [18].

If $n > m$, $\mathbf{C}$ is no longer a square matrix and the approximation can not fit all the u_j^h values. This problem can be simply overcome by determining the $\hat{u}$ values by minimizing the sum of the square distances of the error at each point weighted with a function $\varphi(x)$ as

$$J = \sum_{j=1}^{n} \varphi(x_j)(u_j^h - \hat{u}(x_j))^2 = \sum_{j=1}^{n} \varphi(x_j)(u_j^h - \mathbf{p}_j^T \boldsymbol{\alpha})^2 \tag{5}$$

with respect to the $\boldsymbol{\alpha}$ parameters. Note that for $\varphi(x) = 1$ the standard least square (LSQ) method is reproduced.

Function $\varphi(x)$ is usually built in such a way that it takes a unit value in the vicinity of the point i typically called "star node" where the function (or its derivatives) are to be computed and vanishes outside a region Ω_i surrounding the point. The region Ω_i can be used to define the number of sampling points n in the interpolation region. A typical choice for $\varphi(x)$ is the normalized Gaussian function and this has been chosen in the examples shown in Sections 5.1-5.3. Of course $n \geq m$ is always required in the sampling region and if equality occurs no effect of weighting is present and the interpolation is the same as in the LSQ scheme.

Standard minimization of eq.(5) with respect to $\boldsymbol{\alpha}$ gives

$$\boldsymbol{\alpha} = \bar{\mathbf{C}}^{-1}\mathbf{u}^h \qquad , \qquad \bar{\mathbf{C}}^{-1} = \mathbf{A}^{-1}\mathbf{B} \tag{6}$$

$$\begin{aligned} \mathbf{A} &= \sum_{j=1}^{n} \varphi(x_j)\mathbf{p}(x_j)\mathbf{p}^T(x_j) \\ \mathbf{B} &= [\varphi(x_1)\mathbf{p}(x_1), \varphi(x_2)\mathbf{p}(x_2), \cdots, \varphi(x_n)\mathbf{p}(x_n)] \end{aligned} \tag{7}$$

The final approximation is obtained by substituting $\boldsymbol{\alpha}$ from eq.(6) into (1) giving

$$\hat{u}(x) = \mathbf{p}^T\bar{\mathbf{C}}^{-1}\mathbf{u}^h = \mathbf{N}^T\mathbf{u}^h = \sum_{j=1}^{n} N_j^i u_j^h \tag{8}$$

where the "shape functions" are

$$N_j^i(x) = \sum_{l=1}^{m} p_l(x)\bar{C}_{lj}^{-1} = \mathbf{p}^T(x)\bar{\mathbf{C}}^{-1} \tag{9}$$

It must be noted that accordingly to the least square character of the approximation

$$u(x_j) \simeq \hat{u}(x_j) \neq u_j^h \tag{10}$$

i.e. the local values of the approximating function do not fit the nodal unknown values (Figure 1). Indeed $\hat{u}$ is the true approximation for which we shall seek the satisfaction of the differential equation and the boundary conditions and u_j^h are simply the unknown parameters sought.

The weighted least square approximation described above depends on a great extend on the shape and the way to apply the weighting function. The simplest way is to define a fixed function $\varphi(x)$ for each of the Ω_i interpolation domains (see Figure 1) [11,12].

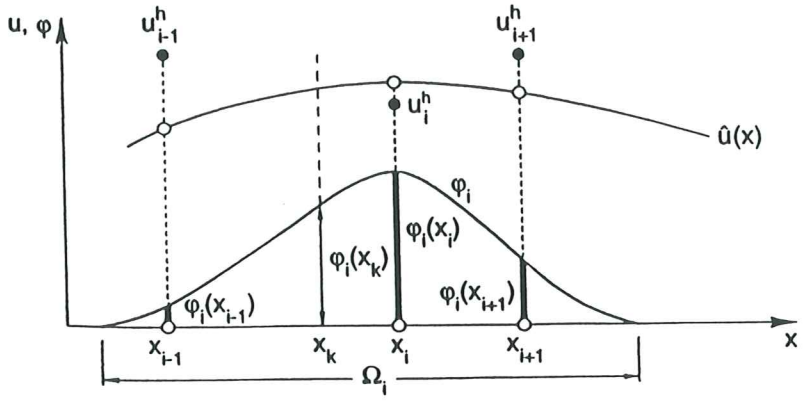

Figure 1. Fixed weighing least square procedure.

Let $\varphi_i(x)$ be a weighting functions satisfying (Figure 1)

$$\begin{cases} \varphi_i(x_i) = 1 \\ \varphi_i(x) \neq 0 \ x \in \Omega_i \\ \varphi_i(x) = 0 \ x \notin \Omega_i \end{cases} \tag{11}$$

Then the minimization square distance becomes

$$J_i = \sum_{j=1}^{n} \varphi_i(x_j)(u_j^h - \hat{u}(x_j))^2 \quad \text{minimum} \tag{12}$$

The expression of matrices $\mathbf{A}$ and $\mathbf{B}$ coincide with eq.(7) with $\varphi(x_j) = \varphi_i(x_j)$

Note that according to (1), the approximate function $\hat{u}(x)$ is defined in each interpolation domain Ω_i. In fact, different interpolation domains can yield different shape functions N_j^i. As a consequence a point belonging to two or more overlapping interpolation domains has different values of the shape functions which means that $N_j^i \neq N_j^k$. The interpolation is now multivalued within Ω_i and, therefore for any useful approximation a decision must be taken limiting the choice to a single value. Indeed, the approximate function $\hat{u}(x)$ will be typically used to provide the value of the unknown function $u(x)$ and its derivatives in only specific regions within each interpolation domain. For instance by using point collocation we may limit the validity of the interpolation to a single point x_i. It is precisely in this context where we have found this meshless method to be more useful for practical purposes [10–13].

Discretization of governing equations

Let us assume a problem governed by the following set of differential equations

$$A(u_j) = 0 \qquad \text{in } \Omega$$

with boundary conditions

$$\begin{aligned} u_j - \bar{u}_j &= 0 \qquad \text{on } \Gamma_u \\ B(u_j) &= 0 \qquad \text{on } \Gamma_t \end{aligned} \tag{13}$$

In above A is a differential operator defining the governing differential equations to be satisfied on the domain Ω with boundary $\Gamma = \Gamma_t \cup \Gamma_\phi$, B is the differential operator defining the boundary conditions at the Neumann boundary Γ_t, u_j are the unknown variables with prescribed values $\bar{u}_j$ at the boundary Γ_u, $j = 1, 2, \cdots, N_v$ where N_v is the number of variables.

A stabilized form of above differential equations can be found by using the *finite increment calculus* (FIC) procedure described in [14–17]. The FIC method is based on imposing the balance laws typical of solid and fluid mechanics over a domain of finite size and retaining higher order terms in the standard Taylor series expansion used to approximate the unknown field over the balance domain. The stabilized form of eqs. (13) reads

$$\begin{aligned} A - \underline{\frac{1}{2} h_j \frac{\partial A}{\partial x_j}} &= 0 \qquad \text{in } \Omega \\ u_j - \bar{u}_j &= 0 \qquad \text{on } \Gamma_u \\ B - \underline{\frac{1}{2} h_j n_j A} &= 0 \qquad \text{on } \Gamma_t \end{aligned} \tag{14}$$

where n_j are the components of the unit normal to the boundary Γ_t and h_j are the dimensions of the balance domain (also called characteristic length parameters). The underlined terms in eq.(14) introduce the necessary stabilization in the governing equations at discrete level. It can be shown that eqs.(14) are the starting point for deriving many well known stabilized numerical methods typically used in computational fluid dynamic problems [14–17]. The stabilized equations (2) have also been found useful for enhanced application of the FPM in solid and fluid mechanics [13].

The discretized system of equations in the FPM is found by substituting the approximation (8) into eqs.(14) and collocating the

differential equations at each point in the analysis domain. This gives

$$\left[A(\hat{u}_j) - \frac{1}{2}h_j \frac{\partial}{\partial x_j} A(\hat{u}_j)\right]_k = 0 \qquad k = 1, 2 \cdots N_t$$

$$[\hat{u}_j]_s - \bar{u}_j = 0 \qquad s = 1, 2 \cdots N_s \tag{15}$$

$$\left[B(\hat{u}_j) - \frac{1}{2}h_j n_j A(\hat{u}_j)\right]_p = 0 \qquad p = 1, 2 \cdots N_t$$

In above N_t is the number of points within the domain Ω and N_s and N_t are the points located on the boundaries Γ_u and Γ_t, respectively.

The discretized system of equations (15) can be written in the standard matrix form

$$\mathbf{K}\mathbf{u}^h = \mathbf{f} \tag{16}$$

from where the values of the nodal parameters u_i^h can be found.

Details of the implementation of the boundary conditions on the Dirichlet boundary Γ_t are given in [11,12].

The computation of the characteristic length parameters h_i follows the procedure explained in [13–17]. In the examples shown in the paper using quadratic base functions, the value $h_i = d_i^{\min}$ has been chosen where $d_i^{\min}$ is the closest distance from a star node in a cloud to its closest neighbour.

Further details on the FPM can be found in [10–13].

3. ROTATION FREE SHELL TRIANGLES

The development of simple and efficient plate and shell triangles is still a challenge in computational structural mechanics. Traditional elements based on Kirchhoff's thin plate theory have the drawback of C_1 continuity requirements whereas more advanced elements based on Reissner-Mindlin's hypothesis suffer from shear locking deffects [18].

Several authors have tried to derive plate and shell finite elements with displacements as the only nodal variables [19–25]. Most of these developments assume that the elements are hinged together at their common boundaries and the bending stiffness is represented by torsional springs placed at the hinge lines.

Oñate and Cervera [26] derived a simple rotation-free thin plate triangle based on combining finite element approximations with finite volume (FV) concepts [27]. The approach has been formalized in [28] using a mixed Hu-Washizu formulation and extended to the derivation of new rotation-free thin plate and shell triangles. Applications of the new rotation-free shell triangles to engineering shell analysis, sheet stamping and contact-impact problems were reported in [28–31].

The basis of the combined FE-FV procedure for deriving rotation free thin plate bending elements is briefly described next.

Let us consider the plate of Figure 2. We will assume Kirchhoff's condition to hold. The set of governing equations is expressed in integral form starting from the standard Hu-Washizu functional

$$\Pi = \frac{1}{2}\int\int_A \boldsymbol{\kappa}^T \mathbf{D}\boldsymbol{\kappa}\, dA - \int\int_A [\mathbf{L}w - \boldsymbol{\kappa}]^T \mathbf{m}\, dA - \int\int_A qw\, dA \qquad (17)$$

where $\boldsymbol{\kappa}$ and $\mathbf{m}$ are the curvature and bending moment fields, $\mathbf{D}$ is the constitutive matrix, q is the distributed load, w is the vertical deflection and A the area of the plate. The form of above matrices and vectors is shown in Figure 2 where all simbols have the standard meaning.

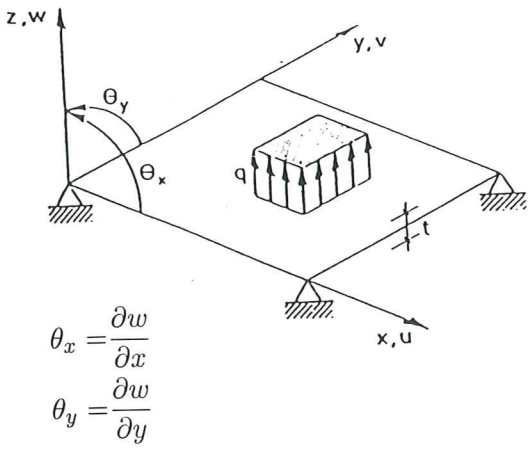

$$\theta_x = \frac{\partial w}{\partial x}$$

$$\theta_y = \frac{\partial w}{\partial y}$$

$$\boldsymbol{\kappa} = \mathbf{L}w$$

$$\mathbf{L} = \left[-\frac{\partial^2}{\partial w^2}, -\frac{\partial^2}{\partial y^2}, -2\frac{\partial^2}{\partial x \partial y}\right]^T$$

$$\mathbf{m} = [M_x, M_y, M_{xy}]^T$$

$$\mathbf{D} = \frac{E}{1-\nu^2}\begin{bmatrix} 1 & \nu & 0 \\ \nu & 1 & 0 \\ 0 & 0 & \frac{1-\nu}{2} \end{bmatrix}$$

Figure 2. Definition of deflection and rotations in a plate. Basic vectors and matrices.

Variations of Π with respect to $\boldsymbol{\kappa}$, $\mathbf{m}$ and w leads to the following three equations:

$$\textit{Constitutive equation:} \int\int_A \delta\boldsymbol{\kappa}^T [\mathbf{D}\boldsymbol{\kappa} - \mathbf{m}] dA = 0 \qquad (18a)$$

$$\textit{Curvature-deflection equation:} \int\int_A \delta\mathbf{m}^T [\mathbf{L}w - \boldsymbol{\kappa}] dA = 0 \qquad (18b)$$

Equilibrium equation: $$\int\int_A [\mathbf{L}\delta w]^T \mathbf{m} dA - \int\int_A \delta w q dA = 0 \qquad (18c)$$

Let us consider an arbitrary discretization of the plate into standard three node triangles. The curvature and the bending moments are described by constant fields within appropriate *non-overlapping control domains* covering the whole plate as

$$\mathbf{m} = \mathbf{I}_3 \mathbf{m}_p, \qquad \delta\mathbf{m} = \mathbf{I}_3 \delta\mathbf{m}_p \qquad (19a)$$

$$\boldsymbol{\kappa} = \mathbf{I}_3 \boldsymbol{\kappa}_p, \qquad \delta\boldsymbol{\kappa} = \mathbf{I}_3 \boldsymbol{\kappa}_p \qquad (19b)$$

where $\mathbf{I}_3$ is the 3×3 unit matrix and $(\cdot)_p$ denotes constant values for the p-th control domain.

Two modalities of control domains are considered: a) that formed by a single triangular element (Figure 3a) and b) the control domain formed by 1/3 of the areas of the elements surrounding a node (Figure 3b). The two options are termed in the FV literature "cell centered" and "cell vertex" schemes, respectively. Note that in the cell centered scheme each control domain coincides with a standard three node finite element triangle. Alternatively in the cell vertex scheme an element is formed by contributions from three different control domains.

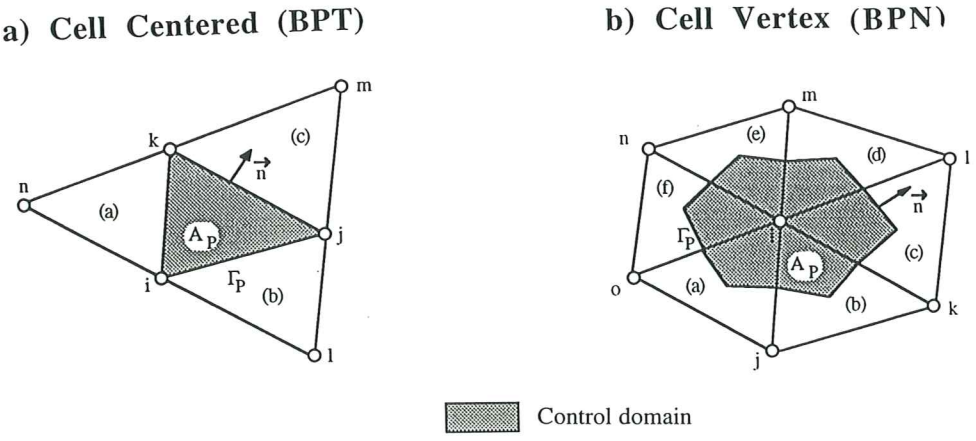

Figure 3. a) Cell centered and cell vertex schemes; b) BPT and BPN elements

It is also useful to define the term "patch of elements" associated to a control domain. In the cell centered scheme this patch is always formed by four elements (except at the boundaries), whereas in the cell vertex scheme the number of elements in the patch is variable.

Derivation of the curvature and bending moment fields as well as the stiffness matrix of each control domain will be expressed next in terms of the nodal deflections associated to the corresponding element patch.

The area integrals in eqs.(18) can be written as sum of contributions over the different control domains taking into account eqs. (19) as

$$\textit{Constitutive equation: } \sum_p \int\int_{A_p} \delta\boldsymbol{\kappa}_p^T[\mathbf{D}\boldsymbol{\kappa}_p - \mathbf{m}_p]dA = 0 \tag{20}$$

where A_p is the area of the p-th control domain. Recalling that the virtual curvatures are arbitrary, gives

$$\boxed{\mathbf{m}_p = \mathbf{D}_p\boldsymbol{\kappa}_p} \tag{21}$$

where $\mathbf{D}_p = \frac{1}{A_p}\int\int_{A_p}\mathbf{D}dA$ is the average constitutive matrix over a control domain.

$$\textit{Curvature-deflection equation: } \sum_p \int\int_{A_p} \delta\mathbf{m}_p^T[\mathbf{L}w - \boldsymbol{\kappa}_p]dA = 0 \tag{22}$$

Taking into account that the virtual bending moments are arbitrary, gives

$$\boldsymbol{\kappa}_p = \frac{1}{A_p}\int\int_{A_p}\mathbf{L}w dA \tag{23}$$

A simple integration by parts of the r.h.s. of eq.(23) leads to

$$\boxed{\boldsymbol{\kappa}_p = \frac{1}{A_p}\int_{\Gamma_p}\mathbf{T}\boldsymbol{\nabla}w d\Gamma} \quad \text{where} \quad \mathbf{T} = \begin{bmatrix} n_x & 0 & n_y \\ 0 & n_y & n_x \end{bmatrix}^T, \qquad \boldsymbol{\nabla} = \begin{Bmatrix} \frac{\partial}{\partial x} \\ \frac{\partial}{\partial y} \end{Bmatrix} \tag{24}$$

and $\mathbf{n} = [n_x, n_y]^T$ is the outward unit normal to the boundary Γ_p surrounding the control domain (Figure 3).

Eq.(24) defines the curvatures for each control domain in terms of the deflection gradients along its boundaries. The transformation of the area integral of eq.(23) into a line integral is typical of finite volume (FV) methods [27].

Integrating by parts the first integral in eq. (18c), gives

$$\sum_p \int_{\Gamma_p} [\mathbf{T}\nabla\delta w]^T \mathbf{m}_p d\Gamma - \int\int_A \delta w q dA = 0 \tag{25}$$

Substituting eqs.(21) and (23) into (25) gives finally

$$\boxed{\sum_p \int_{\Gamma_p} [\mathbf{T}\nabla\delta w]^T \frac{1}{A_p} \mathbf{T}\nabla w d\Gamma - \int\int_A \delta w q dA = 0} \tag{26}$$

The final step is to discretize the deflection field. The simplest option is to interpolate linearly the deflection within each triangular element in terms of the nodal deflections in the standard finite element manner as

$$w = \sum_{i=1}^{3} N_i w_i = \mathbf{N}^{(e)} \boldsymbol{w}^{(e)} \tag{27}$$

with $\mathbf{N}^{(e)} = [N_1, N_2, N_3]$ and $\boldsymbol{w}^{(e)} = [w_1, w_2, w_3]^T$. In (27) w_i denotes nodal deflection values and N_i are the standard linear shape functions of the three node triangle [18].

Substituting eq. (27) into (26) gives the final system of algebraic equation as

$$\mathbf{K}\boldsymbol{w} = \mathbf{f} \tag{28}$$

where vector $\boldsymbol{w}$ contains the nodal deflections. The stiffness matrix $\mathbf{K}$ can be obtained by assembling the contributions from the different control domains given by

$$\mathbf{K}_p = [\mathbf{B}_p]^T \mathbf{D} \mathbf{B}_p A_p \tag{29}$$

where $\mathbf{B}_p$ is the curvature matrix relating the constant curvature field within a control domain and the nodal deflections associated to the corresponding patch of triangles.

3.1 Cell centered patch. BPT element

The evaluation of the constant curvature field in eq.(23) requires the computation of the deflection gradients along the control domain boundaries. This poses a difficulty in cell centered configurations where each control domain coincides with an individual element (Figure 3a). Here if the deflection is linearly interpolated within each element, then the term ∇w is discontinuous at element sides. A simple method

to overcome this problem proposed by Oñate and Cervera [26] is to compute the deflection gradients at the triangle sides as the average value of the gradients contributed by the two elements sharing the side. The constant curvature field for each control domain can be expressed in this case using eq.(23) as

$$\boldsymbol{\kappa}_p = \frac{1}{2A^{(e)}} \int_{\Gamma_p} \mathbf{T}[\nabla \mathbf{N}^{(p)} \boldsymbol{w}^{(p)} + \nabla \mathbf{N}^{(i)} \boldsymbol{w}^{(i)}] d\Gamma = \mathbf{B}_p \boldsymbol{w}_p \qquad (30a)$$

with

$$\boldsymbol{w}_p = [w_i, w_j, w_k, w_l, w_m, w_n]^T \qquad (30b)$$

In eq.(30a) superindexes p and $i = a, b, c$ denote respectively the p-th element and any of the three elements adjacent to element p (Figure 3a).

The resulting plate element is identical to that derived by Oñate and Cervera [26] and is termed BPT (for Basic Plate Triangle). The element can be viewed as a standard finite element plate triangle with one degree of freedom per node and a wider bandwidth, as each element is linked to its neiboughrs through eq.(30a).

3.2 Cell vertex patch. BPN element

As mentioned earlier, a different class of rotation-free plate triangles can be derived starting from the so called cell vertex scheme (Figure 3b). The advantage of the cell vertex scheme is that the deflection gradient is now continuous along the control domain boundaries. This allows to compute directly the curvatures within a control domain as

$$\boldsymbol{\kappa}_p = \frac{1}{A_p} \int_{\Gamma_p} \mathbf{T} \nabla \mathbf{N}_p \boldsymbol{w}_p d\Gamma = \mathbf{B}_p \boldsymbol{w}_p \qquad (31)$$

where $\mathbf{N}_p$ contains contributions from the shape functions from all the elements associated to the p-th control domain. Eq. (31) can be rewritten in a simpler form, taking into account that the deflection gradients are constant within each element, as

$$\boldsymbol{\kappa}_p = \frac{1}{A_p} \sum_i \frac{l_i}{2} \mathbf{T}_i \nabla \mathbf{N}^{(i)} \boldsymbol{w}^{(i)} = \mathbf{B}_p \boldsymbol{w}_p \qquad (32)$$

where the sum extends over all the elements contributing to the p-th control domain, l_i is the exterior side of element i in the patch and $A_p = \frac{1}{3} \sum_i A^{(i)}$.

It is important to note that $\mathbf{B}_p$ is in this case the *global curvature matrix* for the central p-th node. Thus, the product $\mathbf{B}_p^T \mathbf{D}_p \mathbf{B}_p \mathbf{A}_p$ provides the p-th row of the global stiffness matrix. This simplifies the assembly and solution process as the global stiffness equations for a node can be elliminated once they are computed.

This element is termed BPN (for Basic Plate Nodal patch). Note that the concept of "element" is generalized in this case as the BPN element combines an standard finite element interpolation with non-standard integration domains.

The implementation of the boundary conditions in the BPT and BPN plate elements is simple and the main difference with standard finite elements is that the conditions on the prescribed rotations must be imposed when the curvature matrices $\mathbf{B}_p$ are being built. Full details can be found in [27,31].

3.3 Basic shell triangle (BST) element

The BPT element of Section 3.1 can be combined with the standard Constant Strain Triangle (CST) to model membrane behaviour. The resulting rotation free shell element is termed BST (for Basic Shell Triangle) (Figure 4). The (constant) local curvatures within each control domain are written in terms of the (local) deflection gradients at the domain edges by means of expressions equivalent to eq.(30a). These gradients are in turn expressed in terms of the deflection values for the adjacent elements sharing each side. A transformation of the local bending stiffness matrix to global axes is then performed for assembly with the in-plane contributions from the CST element in the standard manner [31].

3.4 Basic shell nodal patch (BSN) element

The BPN plate element of Section 3.2 and the CST membrane element can be combined to give the rotation free BSN shell element (Figure 4). The constant curvature and bending moment fields are defined now in nodal axes. The application of eq.(31) requires a transformation of the rotations from nodal to element axes for each of the elements forming the patch. Details can be found in [31].

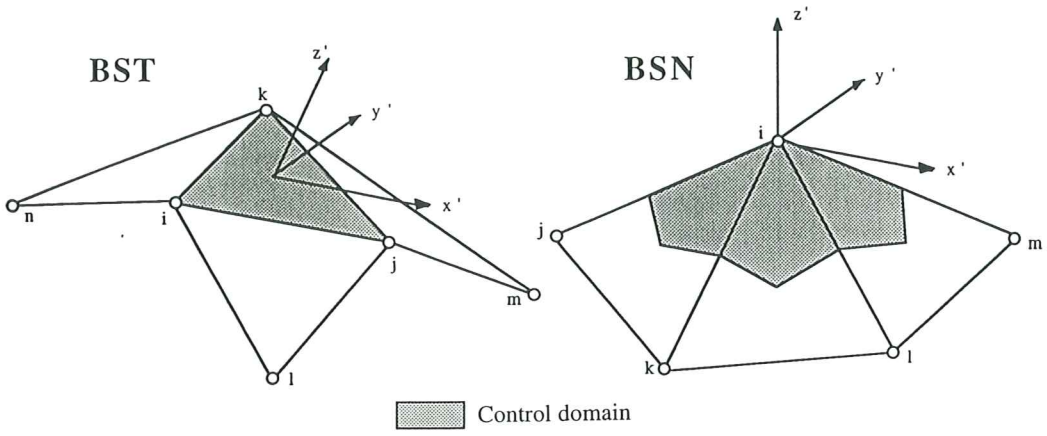

Figure 4. BST and BSN control domains for rotation free shell analysis.

4. A SIMPLE METHOD ALLOWING FREE MOVEMENT OF MESH NODES

Finite element solution of problems such as shape optimization or fluid-structure interaction usually requires the update of the analysis mesh. A typical example is the study of movement of an object within a flowing liquid where the fluid mesh needs to be continuously updated accordingly to the changes in position of the object due to the interaction forces.

Chiandussi, Bugeda and Oñate [32] have recently proposed a simple method for movement of mesh nodes ensuring minimum element distorsion. The method is based on the iterative solution of a fictitions linear elastic problem on the mesh domain. In order to minimize mesh deformation the "elastic" properties of each mesh element are appropiately selected so that elements suffering greater movements are stiffer. The basis of the method is given below.

Let us consider an elastic domain with homogeneous isotropic elastic properties characterized by the Young modulus $\bar{E}$ and the Poisson coefficient ν. Once a discretized finite element problem has been solved using, for instance, standard C_o linear triangles (2D) or linear tetraedra (3D), the principal stresses ${}^1\sigma_i$ at the center of each element are obtained as

$$ {}^1\sigma_i = \bar{E}[\varepsilon_i - \nu(\varepsilon_j + \varepsilon_k)] \qquad i,j = 1,2,3 \ \text{ for 3D} \tag{33} $$

where ε_i are the principal strains.

Let us assume now that a uniform strain field $\varepsilon_i = \bar{\varepsilon}$ throughout

the mesh is sougth. The principal stresses are then given by

$$^2\sigma_i = E\bar{\varepsilon}(1-2\nu) \qquad i = 1,2,3 \ \text{ for 3D} \tag{34}$$

where E is the unknown Young modulus for the element.

A number of criteria can be now used to find the value of E. The most effective approach found in [32] is to equal the element strain energies in both analysis. Thus

$$U_1 = {}^1\sigma_i\varepsilon_i = \bar{E}[(\varepsilon_1^2+\varepsilon_2^2+\varepsilon_3^2) - 2\nu(\varepsilon_1\varepsilon_2+\varepsilon_2\varepsilon_3+\varepsilon_1\varepsilon_3)] \tag{35}$$

$$U_2 = {}^2\sigma_i\varepsilon_i = 3E\bar{\varepsilon}^2(1-2\nu) \tag{36}$$

Equaling eqs.(35) and (36) gives the sought Young modulus E as

$$E = \frac{\bar{E}}{3\bar{\varepsilon}^2(1-2\nu)}[(\varepsilon_1^2+\varepsilon_2^2+\varepsilon_3^2) - 2\nu(\varepsilon_1\varepsilon_2+\varepsilon_2\varepsilon_3+\varepsilon_1\varepsilon_3)] \tag{37}$$

Note that the element Young modulus is proportional to the element deformation as desired. Also recall that both $\bar{E}$ and $\bar{\varepsilon}$ are constant for all elements in the mesh.

The solution process includes the following two steps.

Step 1. Consider the finite element mesh as a linear elastic solid with homogeneous material properties characterized by $\bar{E}$ and ν. Solve the corresponding elastic problem with imposed displacements at the mesh boundary. These displacements can be due to a prescribed motion of a body within a fluid, to changes in the shape of the domain in an optimum design problem, etc.

Step 2. Compute the principal strains and the values of the new Young modulus in each element using eq.(37) for a given strain field $\bar{\varepsilon}$. Repeat the finite element solution of the linear elastic problem with prescribed boundary displacements using the new values of E for each element.

The movement of the mesh nodes obtained in the second step ensures a quasi uniform mesh distorsion. Further details on this method including other alternatives for evaluating the Young modulus E can be found in [32].

5. EXAMPLES

5.1 Example 1. Inviscid incompressible flow around a NACA profile using the FPM

Figure 5 shows the geometry of the NACA profile and the distribution of 5300 points used for the analysis using the Finite Point Method (FPM). The steady-state solution of the incompressible Euler equations has been found using a fractional step procedure described in [33,34,17]. A quadratic interpolation for velocities and pressure ($m = 6$) within clouds of $n \geq 6$ points has been used. Numerical results for the velocity and pressure contours for an angle of attack of 5^o and $u_\infty = 1$ are shown in Figure 5. A plot of the C_d coefficient is also presented.

5.2 Example 2. Analysis of a simple supported beam using the FPM

Figure 6a shows the geometry of the beam, the mechanical properties and the uniform distribution of 105 points. A point load acting on the free edge is considered. Again a quadratic interpolation for the displacement variables has been chosen. Numerical results for the beam deflection and the stress distribution are shown in Figures 6d and 6e. The same problem has been analyzed with the FEM using a structured mesh of 150 linear plane stress triangles (CST element) based on the same point distribution (Figure 6c). Nodal stresses have been obtained by standard nodal averaging of element values. Comparison of the errors for the control deflection and the maximum σ_x stress gives some advantage to the FPM results.

5.3 Example 3. Square plate with circular hole under tension

Figure 7 shows the geometry of the plate and the loading. One quater of the plate is analyzed only due to symmetry. The problem has been solved with the FPM using an unstructured grid of 148 points. Contours of the horizontal displacement and the σ_x stress obtained with the FPM are shown. Results for the maximum σ_x stress at the upper tip of the hole obtained with the FPM are very accurate (1% error). This compares very favourably with the 16% error obtained with the FEM using the unstructured mesh of 58 CST elements shown in Figure 7c. Further applications of the FPM can be found in [10–13].

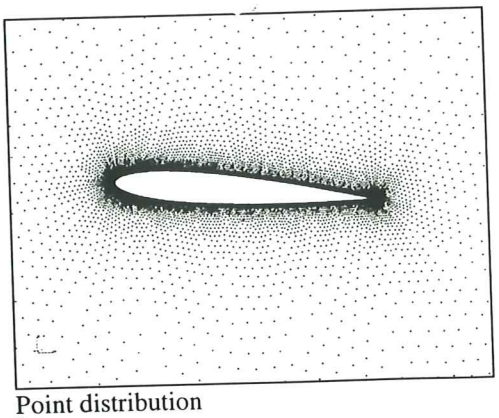

Point distribution

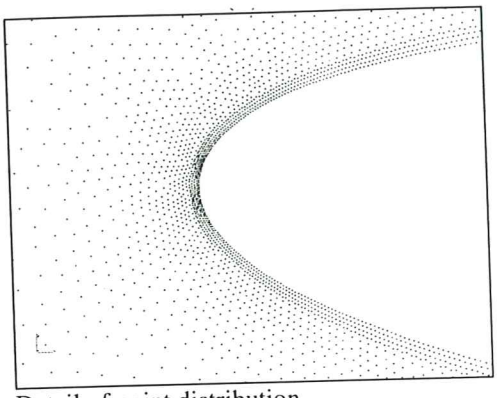

Detail of point distribution

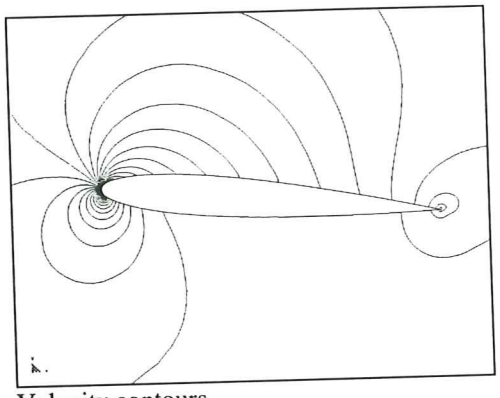

Velocity contours

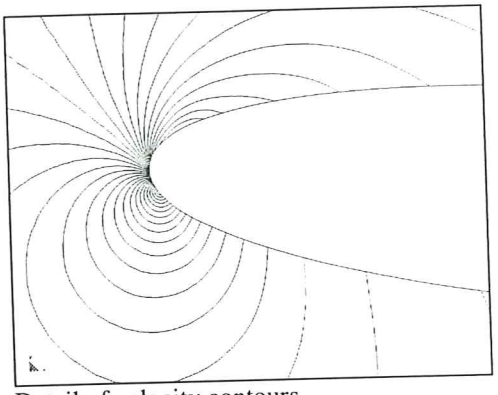

Detail of velocity contours

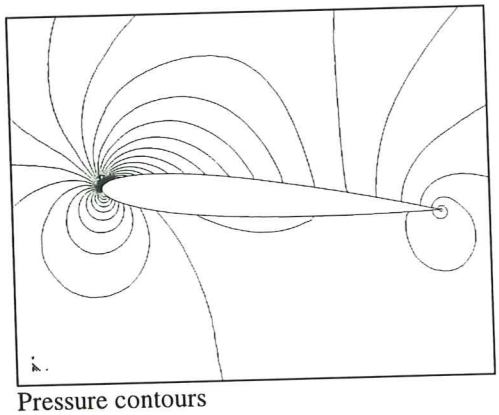

Pressure contours

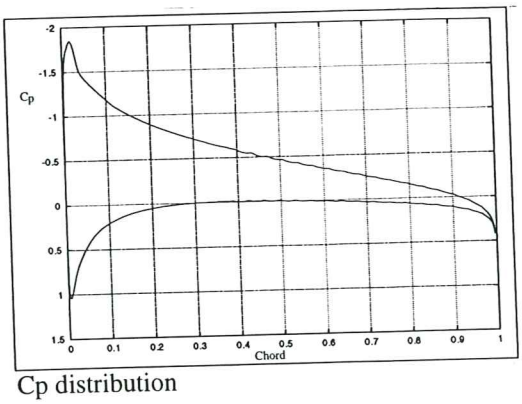

Cp distribution

Figure 5. Inviscid solution around NACA0012 profile. Angle of attack, $\alpha = 5^o, u_\infty = 1$.

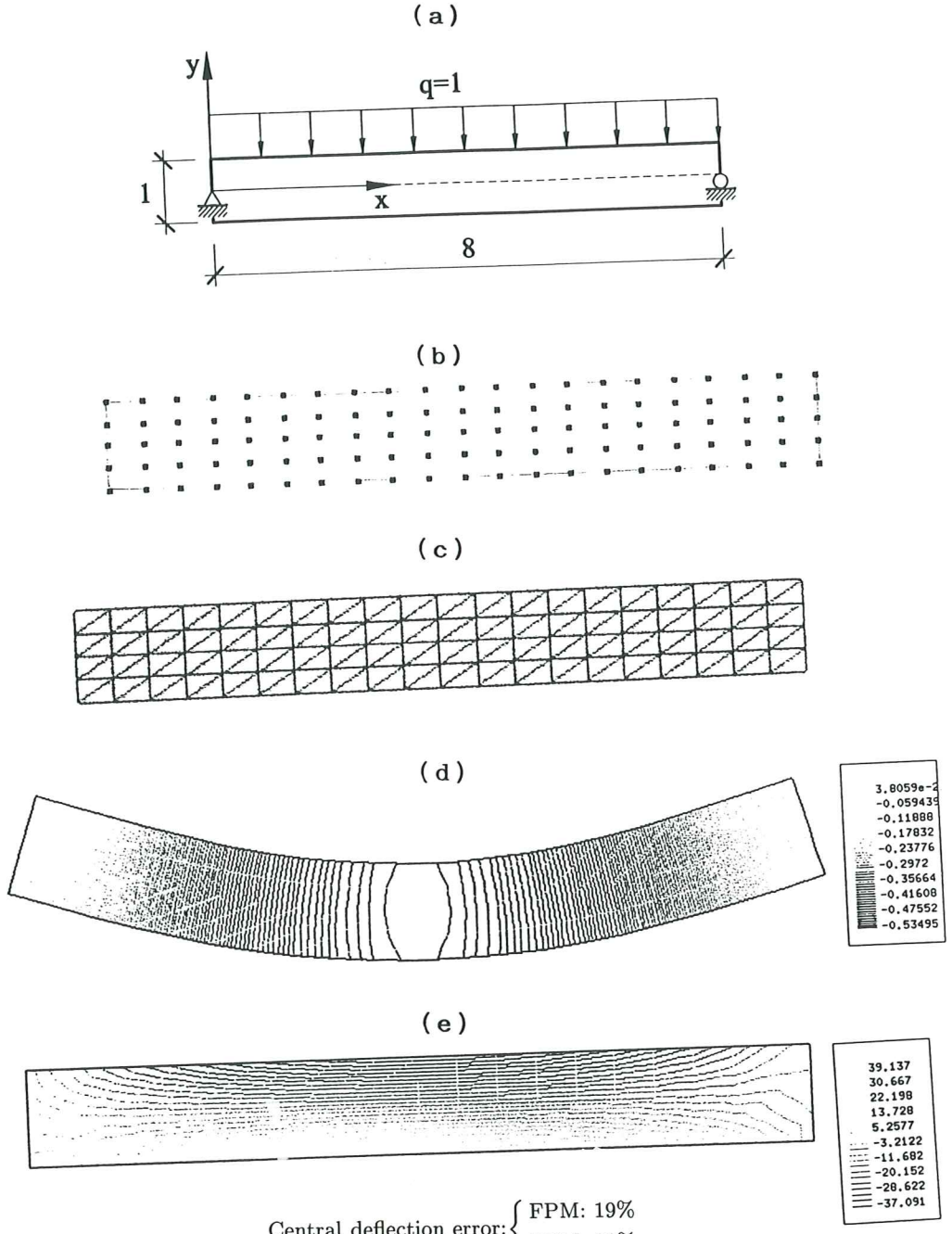

Central deflection error: { FPM: 19% / FEM: 21% }

Error in maximum σ_x stress: { FPM: 19% / FEM: 38% }

Figure 6. Simple supported beam analyzed with FPM and FEM. a) Beam geometry and loading. b) Structured grid of 105 points. c) Structured mesh of 160 CST elements. d) Deflection field (FPM). e) σ_x stress field (FPM).

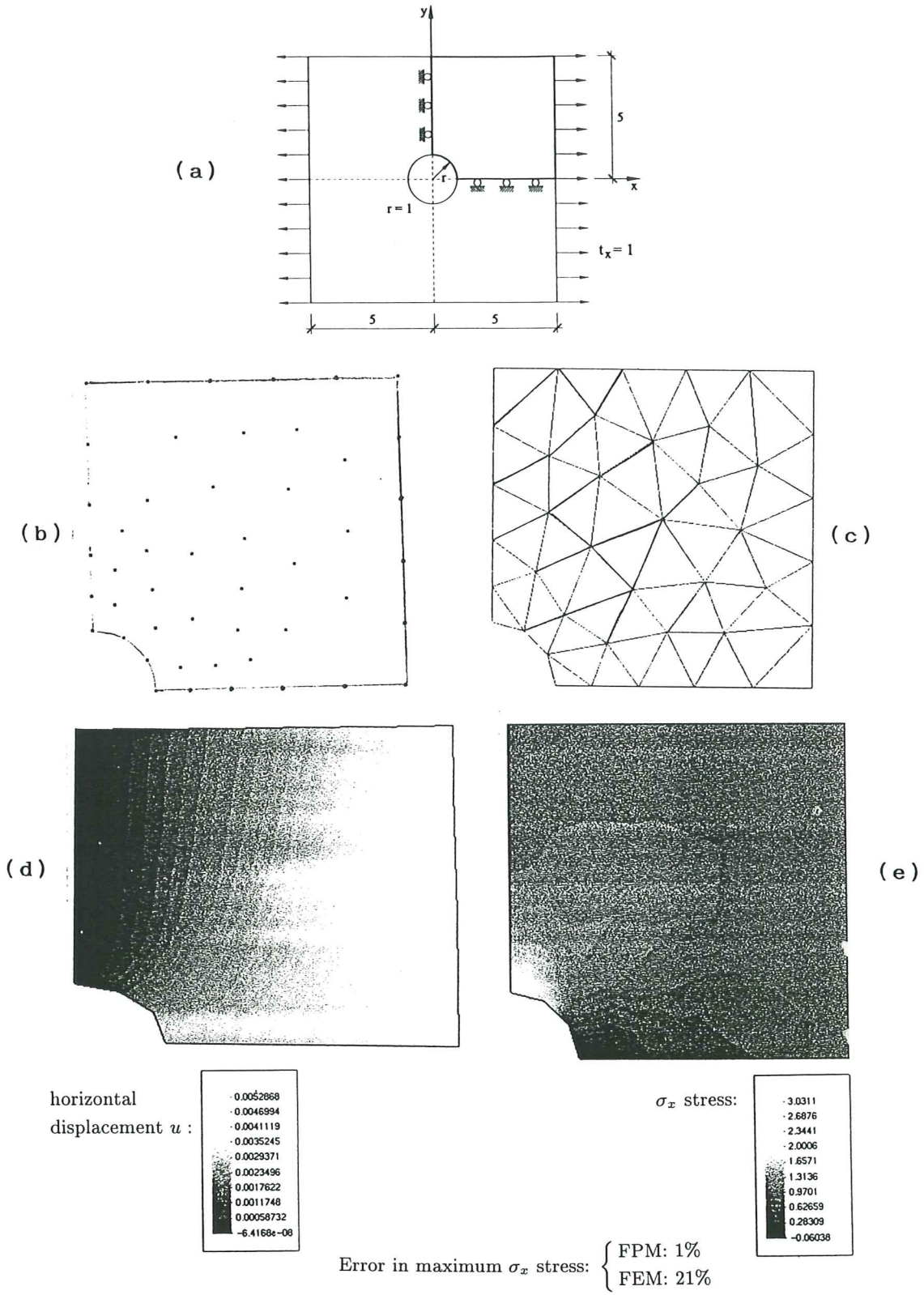

Figure 7. Square plate with circular hole under tension analyzed with FPM and FEM. a) Plate geometry and loading. b) Unstructured grid of 48 points. c) Unstructured mesh of 58 CST elements. d) Horizontal displacement contours (FPM). e) σ_x contours (FPM).

5.4 Example 4. Spherical dome under impulse pressure loading

This example illustrates the efficiency of the new rotation free BST shell element for non linear elastoplastic dynamic analysis of shells using an explicit time integration scheme. The geometry of the dome and the material properties are shown in Figure 8. The loading is due to a uniform pressure of 600 psi acting impulsively. Numerical results for the evolution of the central deflection obtained with three different meshes of BST elements with 507, 867 and 1324 d.o.f. are shown. Note the accuracy of the response for the coarse mesh. A comparison of the results for the 1324 d.o.f. mesh with those obtained with the standard DKT-15 shell element [35] using 1445 d.o.f. is shown in Figure 9.

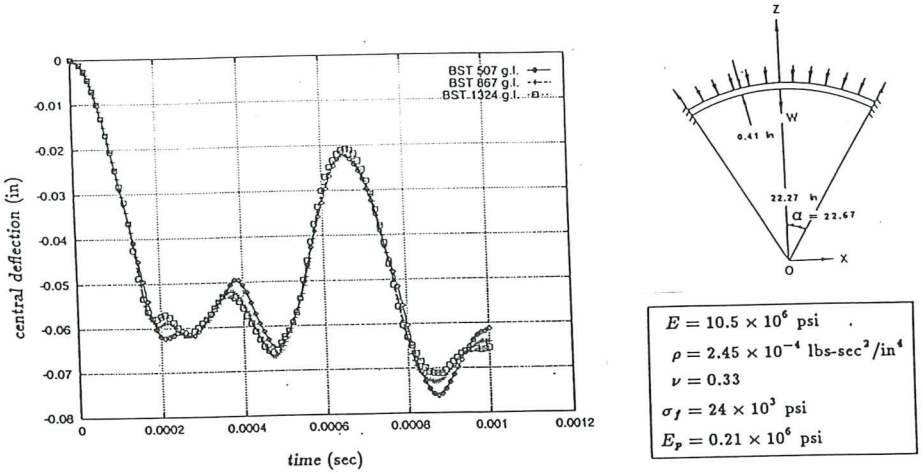

Figure 8. Spherical dome under impulse loading analyzed with the rotation free BST element.

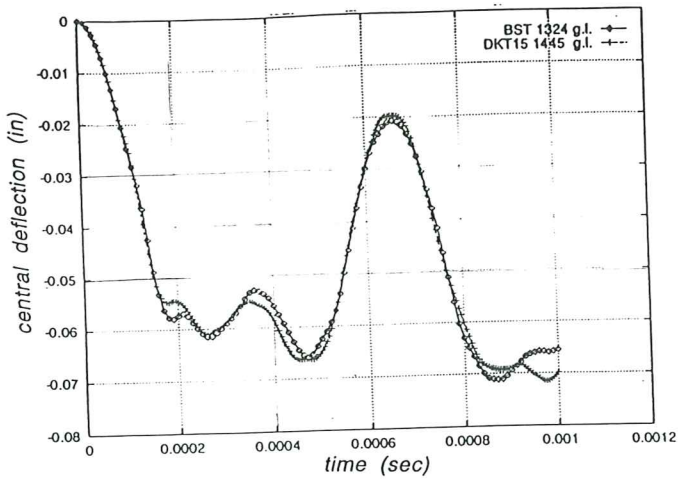

Figure 9. Spherical dome.Comparison of results obtained with BST and DKT15 elements.

5.5 Example 5. Sheet stamping of an industrial part using the rotation free BST triangle

Figures 10a and 10b show the geometry of the die and the mesh of 24683 BST triangles discretizing the sheet. The numerical solution was found using an explicit dynamic code in which the BST element has been implemented [36]. The analysis was run in a parallel PC network under Windows. Figures 10c and 10d show some typical results of the analysis such as the deformed geometry of the sheet after forming and the thickness distribution plotted on the deformed sheet.

Further applications of the BST element can be found in [26–31].

5.6 Example 6. Displacement of an airfoil within a finite element mesh

This example shows the efficiency of the mesh updating procedure presented in Section 4. The problem concerns the change of position of an airfoil within a fluid domain. Figure 11a shows the initial position of the airfoil and the mesh of three node triangles covering the fluid domain. Figures 11b and 11c show the new position of the airfoil after imposing a vertical displacement at the tail end point and a vertical rigid body motion for the whole airfoil, respectively. A value of $\bar{\varepsilon} = 10^{-3}$ was chosen in the analysis. The final airfoil positions correspond to the maximum displacements before element intersection is found in the mesh. A detail of the distorted elements in the vecinity of the airfoil tail is also shown. Note that the final meshes have the same topology than the original ones, i.e. no remeshing has been carried out. Further examples of the mesh free movement procedure proposed can be found in [32].

6. CONCLUDING REMARKS

Some new procedures introducing a higher degree of freedom in standard finite element techniques have been described. The stabilized *finite point method* is a simple fully mesh free procedure which seems a good candidate for solution of practical problems in fluid and solid mechanics. The rotation-free plate and shell elements presented are very adequate for large scale computations in structural engineering and sheet metal forming analysis. Finally the mesh updating procedure described allows to follow large movements of rigid and flexible bodies within fluids without the need of regenerating the mesh.

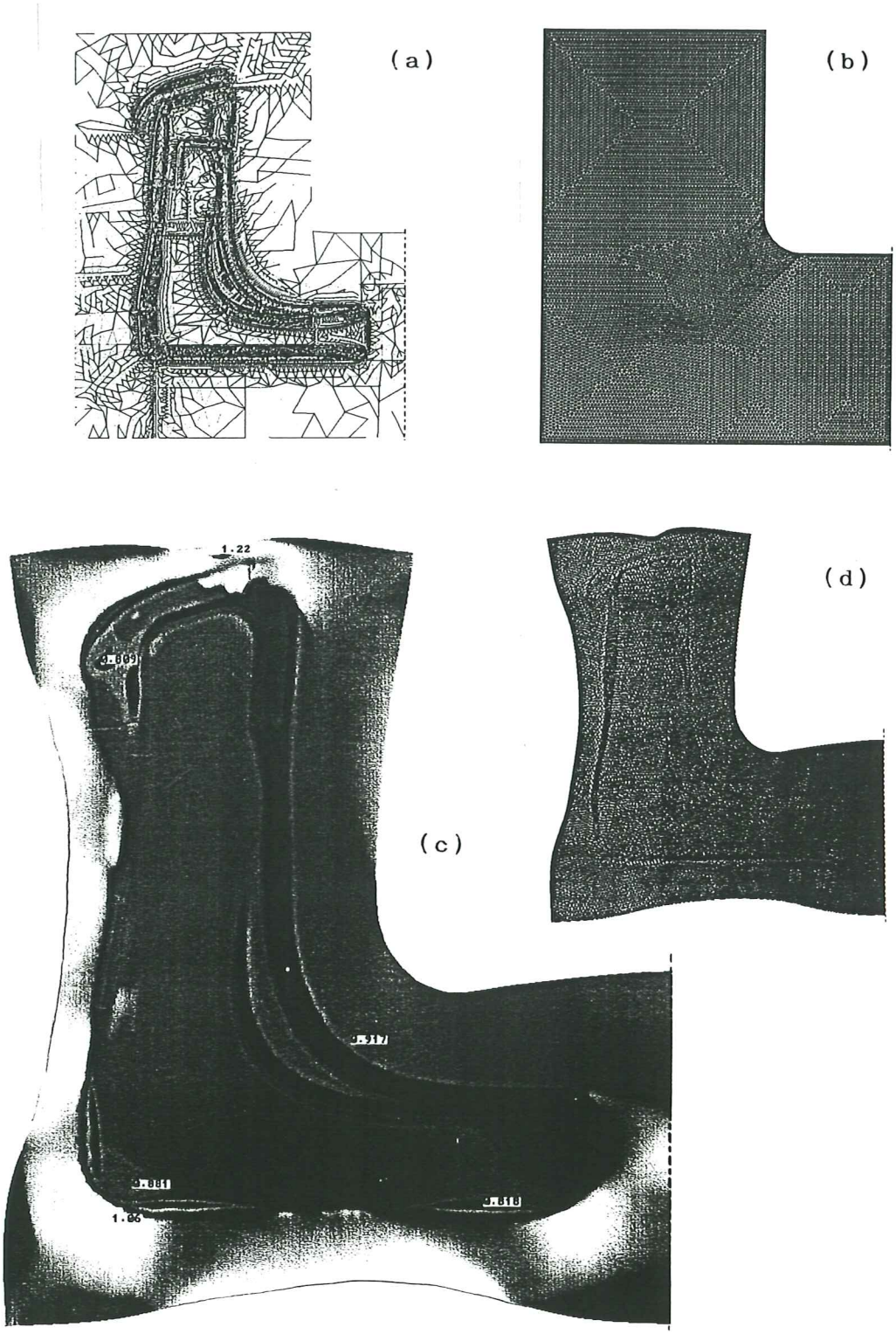

Figura 10. Analysis of an industrial sheet forming process with the BST element. a) Die mesh. b) Sheet discretized in 24683 BST elements. c) Distribution of thickness ratio (t/t_o). d) Deformed sheet mesh after forming.

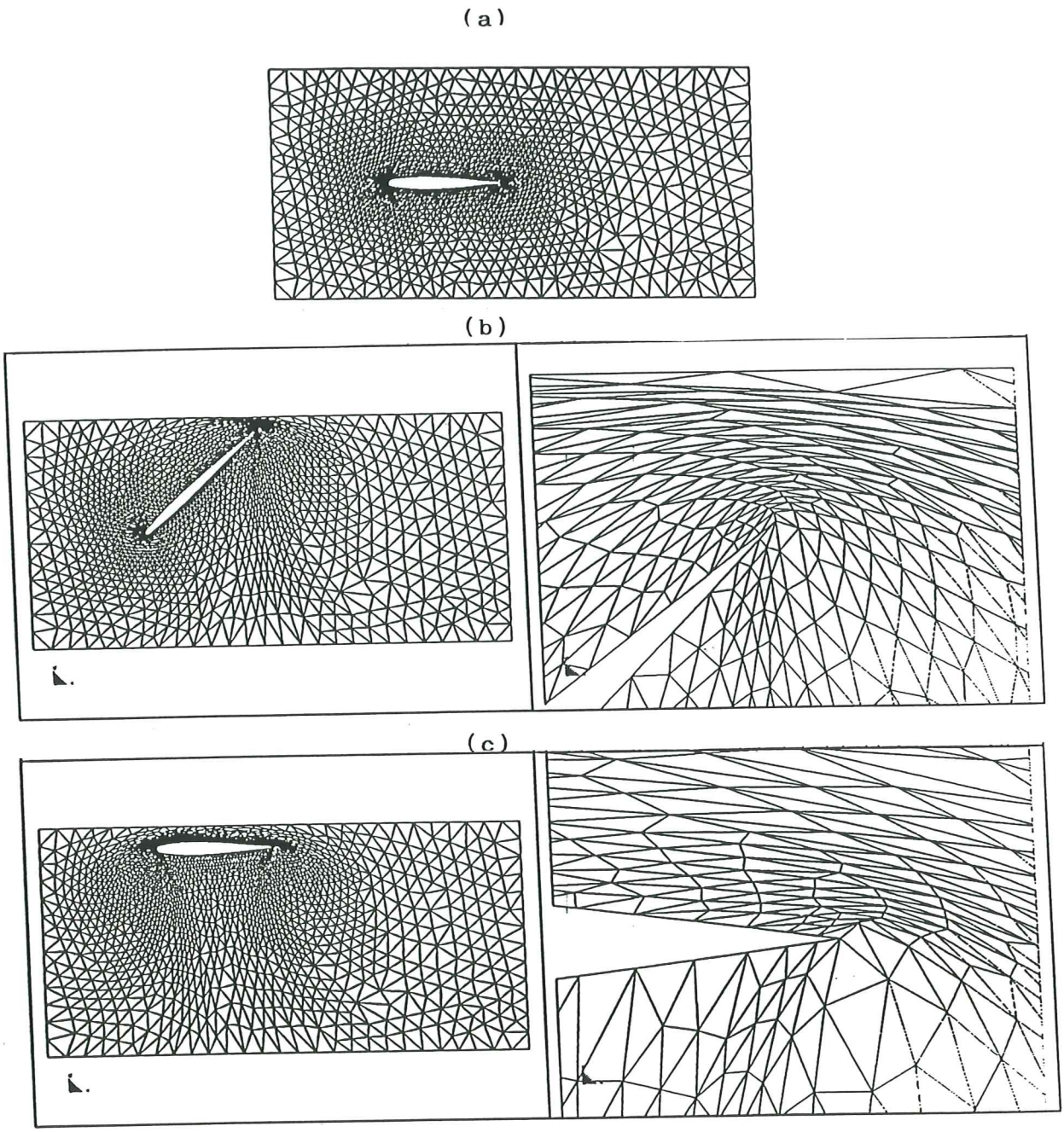

Figura 11. Movement of a NACA0012 airfoil within a fluid domain. a) Initial position of airfoil. Final airfoil position and mesh after: vertical displacement of tail point (b) and vertical rigid body displacement of airfoil (c). Figures show the maximum airfoil displacement before element intersection is found.

ACKNOWLEDGEMENTS

Thanks are given to Mr. Carlos Sacco and Mr. Franco Perazzo who provided the figures for examples 1,2 and 3 respectively. The sheet forming analysis was performed by Ms. Pilar Soler and Ms. Natalia Domínguez from DECAD S.A. using the commercial code STAMPACK [35] with support from QUANTECH ATZ, S.A. Their help is also gratefully acknowledged.

REFERENCES

1. MONAGHAN, J.J. - Smoothed particle hydrodynamics: Some recent improvement and applications. *Annu. Rev. Astron. Physics*, 30, 543, 1992.

2. RANDLES, P.W. and LIBERSKY, L.D. - Smoothed particle hydrodynamics: Some recent improvement and applications. *Appl. Mech. Engng.*, 139, 175, 1996.

3. PERRONE, N. and KAO, R. - A general finite difference method for arbitrary meshes, *Comp. Struct, 5*, 45-47, 1975.

4. LISZKA, T. and ORKISZ, J. - The finite difference method at arbitrary irregular grids and its application in applied mechanics. *Comp. Struct., 11*, 83-95, (1980).

5. NAYROLES, B., TOUZOT, G. and VILLON, P. - Generalizing the FEM: Diffuse approximation and diffuse elements. *Comput. Mechanics, 10*, 307-18, 1992.

6. BELYTSCHKO, T., LU, Y. and GU, L. - Element free Galerkin methods. *Int. J. Num. Meth. Engng., 37*, 229-56, 1994.

7. DOLBOW, J. and BELYTSCHKO, T. - An introduction to programming the meshless element free Galerkin method. *Archives of Comput. Meth. in Engng.*, 5 (3), 207–241, 1998.

8. LIU, W.K., JUN, S., LI, S., ADEE, J. and BELYTSCHKO, T. - Reproducing Kernel particle methods for structural dynamics. *Int. J. Num. Meth. Engng., 38*, 1655–1679, 1995.

9. LIU, W.K., CHEN, Y., JUN, S., CHEN, J.S., BELYTSCHKO, T., PAN, C., URAS, R.A. and CHANG, C.T. - Overview and applications of the Reproducing Kernel particle method. *Archives of Comput. Meth. in Engng.*, Vol. 3(1), 3–80, 1996.

10. OÑATE, E., IDELSOHN, S., ZIENKIEWICZ, O.C. and FISHER, T. - A finite point method for analysis of fluid flow problems. Proceedings of the 9th *Int. Conference on Finite Element Methods in Fluids*, Venize, Italy, 15-21, October 1995.

11. OÑATE, E., IDELSOHN, S., ZIENKIEWICZ, O.C. and TAYLOR, R.L. - A finite point method in computational mechanics. Applications to convective transport and fluid flow. *Int. J. Num. Meth. Engng.*, Vol. 39, 3839–3866, 1996.

12. OÑATE, E., IDELSOHN, S., ZIENKIEWICZ, O.C., and TAYLOR, R.L. - A stabilized finite point method for analysis of fluid mechanics's problems. *Comput. Meth. in Appl. Engng*, Vol. 139, 1-4, pp. 315–347, 1996.

13. OÑATE, E. and S. IDELSOHN - A mesh free finite point method for advective-diffusive transport and fluid flow problems. *Computational Mechanics*, 21, 283–292, 1988.

14. OÑATE, E. - Derivation of stabilized equations for advective-diffusive transport and fluid flow problems. *Comput. Meth. Appl. Mech. Engng.*, Vol. 151, 1-2, pp. 233–267, 1998.

15. OÑATE, E., GARCIA, J. and IDELSOHN, S. - Computation of the stabilization parameter for the finite element solution of advective-diffusive problems. *Int. J. Num. Meth. Fluids*, Vol. 25, pp. 1385–1407, 1997.

16. OÑATE, E., GARCIA, J. and IDELSOHN, S. - An Alpha-adaptive approach for stabilized finite element solution of advective-diffusive problems with sharp gradients. *New Adv. in Adaptive Comp. Met. in Mech.*, P. Ladeveze and J.T. Oden (Eds.), Elsevier, 1998.

17. OÑATE, E. - A finite element method for incompressible viscous flows using a finite increment calculus formulation. *Research Report* N. 150, CIMNE, Barcelona, January 1999.

18. ZIENKIEWICZ, O.C. and TAYLOR, R.C. - *The finite element method*, 4th Edition, Vol. 1, McGraw Hill, 1989.

19. BARNES, M.R. - Form finding and analysis of tension space structure by dynamic relaxation. *Ph.D. Thesis*, Dept. of Civil Engineering, The City University, London, 1977.

20. PHAAL, R. and CALLADINE, C.R. - A simple class of finite elements for plate and shell problems. I: Elements for beams and thin plates. *Int.*

J. Num. Meth. Engn., Vol. 35, 955–977, 1992.

21. PHAAL, R. and CALLADINE, C.R. - A simple class of finite elements for plate and shell problems. II: An element for thin shells with only translational degrees of freedom. *Int. J. Num. Meth. Engn.*, Vol. 35, 979–996, 1992.

22. HAMPSHIRE, J.K., TOPPING, B.H.V and CHAN, H.C. - Three node triangular elements with one degree of freedom per node. *Eng. Comput*, Vol. 9, 49–62, 1992.

23. RIO, G., TATHI, B. and LAURENT, H. - A new efficient finite element model of shell with only three degrees of freedom per node. Applications to industrial deep drawing test. in *Recent Developments in Sheet Metal Forming Technoloy*, Ed. M.J.M. Barata Marques, 18th IDDRG Biennial Congress, Lisbon, 1994.

24. BRUNET, M. and SABOURIN, F. - Prediction of necking and wrinkles with a simplified shell element in sheet forming. *Int. Conf. of Metal Forming Simulation in Industry*, Vol. II, pp. 27–48, B. Kröplin (Ed.), 1994.

25. YANG, D.Y., JUNG, D.W., SONG, L.S., YOO, D.J. and LEE, J.H. - Comparative investigation into implicit, explicit and iterative implicit/explicit schemes for simulation of sheet metal forming processes. *NUMISHEET'93*, Eds. Makinouchi, A., Nakamachi, E., Oñate, E. and Wagoner, R.H., RIKEN, 35–42, Tokyo, 1993.

26. OÑATE, E. and CERVERA, M. - Derivation of thin plate bending elements with one degree of freedom per node. *Eng. Comput.* Vol. 10, 543–561, 1993.

27. OÑATE, E., CERVERA, M. and ZIENKIEWICZ, O.C. - A finite volume format for structural mechanics. *Int. J. Num. Meth. Eng.*, 37, 181–201, 1994.

28. E. OÑATE and F. ZARATE - New thin plate and shell triangles with translational degrees of freedom only. Presented at *IUTAM/IACM Symposium "Discretization Methods in Structural Mechanics II"*, Viena, Austria, June 2–6, 1997.

29. OÑATE, E., CENDOYA, P., ROJEK, J. and MIQUEL, J. - A simple thin shell triangle with translational degrees of freedom for sheet stamping analysis. at *3rd International Conference on Numerical Simulation of 3D Sheet Forming Processes (NUMISHEET'96)*, Dearbon, Michigan, USA, 29 Sept. - 3 Oct., 1996

30. OÑATE, E., CENDOYA, P., ROJEK, J. and MIQUEL, J. - Non linear explicit dynamic analysis of shell structures using a simple triangle with translational degrees of freedom only. at the *International Conference on Computational Engineering Science (ICES'97)*, San Jose, Costa Rica, May 4–9, 1996.

31. OÑATE, E. and ZARATE, F. - Rotation-free triangular plate and shell elements. Research Report 149, CIMNE, Barcelona, January 1999. Submitted to *Int. J. Num. Meth. Engng.*

32. CHIANDUSI, G., BUGEDA, G. and OÑATE, E. - A simple method for update of finite element meshes. Research Report 147, CIMNE, Barcelona, January 1999.

33. ZIENKIEWICZ, O.C. and CODINA, R. (1995) - A general algorithm for compressible and incompressible flow. Part I: The split characteristic based scheme. *Int. J. Num. Meth. in Fluids*, 20, 869-85.

34. ZIENKIEWICZ, O.C., MORGAN, K., SATYA SAI, B.V.K., CODINA, R. and VAZQUEZ, M. - A general algorithm for compressible and incompressible flow. Part II: Tests on the explicit form. *Int. J. Num. Meth. in Fluids*, **20**, No. 8-9, 886-913, 1995.

35. BATOZ, J.L., BATHE, K.J and HO, L.W. - A study of three-node triangular plate bending elements. *Int. J. Num. Meth. Engn.*, Vol. 15, 1771–1812, 1980.

36. STAMPACK - An explicit dynamic finite element code for sheet stamping analysis. QUANTECH ATZ S.A., Barcelona 1999.